Thermochimica Acta 755 (2026) 180181

Contents lists available at ScienceDirect

Thermochimica Acta

journal homepage: www.elsevier.com/locate/tca

Deconvolution of superimposing reaction signals from DSC curves in selected Al-Mg-Si-(Cu) alloys by mean-field modeling and HEXRD

Robert Kahlenberg [a,b,*], Georg Falkinger [c], Roman Schuster [d], Bernhard Miesenberger [e], Nicolás García Arango [e], Emad Maawad [f], Erwin Povoden-Karadeniz [e], Benjamin Milkereit [g,h], Ernst Kozeschnik [a]

[a] Institute of Materials Science and Technology, TU Wien, Getreidemarkt 9 1060 Vienna, Austria
[b] Materials Center Leoben Forschung GmbH, Vordernberger Straße 12 8700 Leoben, Austria
[c] AMAG rolling GmbH, Lamprechtshausenerstrasse 61 5282 Ranshofen, Austria
[d] Department of Lithospheric Research, University of Vienna, Josef-Holaubek-Platz 2 1090 Vienna, Austria
[e] Christian Doppler Laboratory for Interfaces and Precipitation Engineering CDL-IPE, Institute of Materials Science and Technology, TU Wien, Getreidemarkt 9 1060 Vienna, Austria
[f] Institute of Materials Physics, Helmholtz-Zentrum Hereon, Max-Planck-Strasse 1 21502 Geesthacht, Germany
[g] Chair of Materials Science, Faculty of Mechanical Engineering and Marine Technology, University of Rostock, Justus-von-Liebig-Weg 2 18059 Rostock, Germany
[h] Competence Centre CALOR, Department Life, Light & Matter, University of Rostock, Albert-Einstein-Str. 25 18059 Rostock, Germany

ARTICLE INFO

Keywords:
Aluminium alloys
DSC
HEXRD
Precipitation kinetics
Mean-field modelling

ABSTRACT

The present work describes a systematic approach to improve mean-field simulations of dissolution and precipitation of precipitates from the late stages in the precipitation sequence in AlMgSiCu alloys for processing simulations. In addition to metastable precipitates, it considers the evolution of two populations (coarse and fine) of the thermodynamically stable phases in EN AW-6061 and EN AW-6016, β-Mg_2Si and Si respectively. The setup is based on two previous publications using heterogeneous nucleation site energies and their distribution. The simulations are calibrated using data from continuous cooling and heating experiments obtained with differential scanning calorimetry (DSC) and high-energy X-ray diffraction (HEXRD). We show that mean-field simulations combined with DSC and HEXRD can provide valuable information to eliminate uncertainties related to, for instance, the thermodynamic description of metastable precipitates. The method described in this paper also delivers very reasonable results for the evolution of the individual phase fractions. It potentially facilitates the assessment of the influence of different types of nucleation sites and their densities.

1. Introduction

The complexity of the earliest structures in 6xxx series alloys and their relevance to the mechanical properties make the initial stages of the precipitation sequence the major focus of many present research activities [1–4]. Consequently, it is not surprising that the overaged conditions involving thermodynamically more stable precipitates (e.g. β-Mg_2Si, Si, Q, β',…), have recently received comparatively less attention. At the same time, these precipitates typically dominate the microstructure evolution during processing until the solutionizing step, and any attempt at a comprehensive processing simulation needs to take them into account. Furthermore, a closer look at these seemingly more straightforward stages in the precipitation sequence leaves some open questions regarding nucleation mechanisms and the proper setup of consistent kinetic mean-field simulations for aluminum alloys.

In a recent publication, Hennum et al [5] experimentally showed that technical (with Fe and Mn) and pure alloys behave very similarly with respect to the precipitation of β-Mg_2Si during cooling after homogenization, in agreement with previous DSC studies [6]. The observed indifference to the presence of Fe and Mn is somewhat surprising given that the preferred nucleation sites for β-Mg_2Si in technical alloys are Fe- and Mn-containing insoluble intermetallics [6,7], which are absent in pure laboratory alloys. In the context of heating experiments, the situation is further complicated because the dissolution reaction of metastable phases overlaps with the formation of stable β-Mg_2Si precipitates [7,8].

* Corresponding author.
E-mail address: robert.kahlenberg@tuwien.ac.at (R. Kahlenberg).

https://doi.org/10.1016/j.tca.2025.180181
Received 23 July 2025; Received in revised form 30 October 2025; Accepted 16 November 2025
Available online 17 November 2025

In contrast, the nucleation of metastable precipitates during cooling appears to be very much affected by the presence of these insoluble intermetallics, more specifically, dispersoids [6,9–11]. This leads to a noticeable difference in the precipitation reaction of metastable phases, as measured in DSC cooling experiments, when comparing pure and technical alloys [6].

Another interesting phenomenon is the precipitation of pure Si. During continuous cooling of binary Al-Si alloys, pure Si forms with various shapes over a wide range of temperatures, resulting in a broad and smooth precipitation peak in DSC cooling measurements [12,13]. While, e.g., grain boundaries are known to be important nucleation sites for pure Si precipitates [14], the majority of these are found within the grains [12,13], presumably at various other heterogeneous nucleation sites (dislocation jogs, subgrain boundaries, etc.). For quickly quenched and highly supersaturated Al-Si alloys, heterogeneous nucleation of Si precipitates from Si clusters has also been discussed in the literature [15, 16].

The inconclusive experimental evidence regarding the preference of different nucleation sites over one another is difficult to address computationally. In the context of mean-field models for solid-state precipitation, classical nucleation theory (CNT) is the most commonly used approach to describe nucleation [17–19]. It has previously proven to be useful for over-aging simulations of Al-Mg-Si alloys [20]. However, the parameterization of CNT for reasonable descriptions of nucleation barriers, rates, and number densities can be challenging. It commonly requires experimental data for calibration, struggles to correctly capture chemistry variations and the thermodynamic descriptions for metastable precipitates can be an additional bottleneck for the reliability of mean-field simulation setups outside verified confidence intervals.

At the same time, mean-field models are computationally fast and useful tools, provided their limits are acknowledged and the results are critically assessed. Hence, while a truly predictive setup without the necessity of any major fitting parameters remains currently unavailable, the present work proposes a practicable and useful concept for process simulations that includes metastable and stable phases in the late stages of the precipitation sequence.

Furthermore, the approach is to a large extent based on DSC and HEXRD data. DSC is a common tool to study precipitation kinetics, but the superposition of single reactions complicates the interpretation severely [6]. The combination of methods outlined herein allows us to deconvolute this superposition of the reactions belonging to the later stages of the precipitation sequence in the investigated alloys. Thus, it improves our current understanding of the rather complex DSC signals and facilitates further model development.

2. Experimental procedure

The two alloys considered in the present work are EN AW-6061 and EN AW-6016 - they are labelled 6061 and 6016 from this point onwards; the compositions are given in Table 1. The „ideal“ composition with reduced Si content is employed for the simulations because some of the Si is incorporated into thermally stable Fe- and Mn-containing phases, which do not contribute to the DSC signal in the present analysis and are, therefore, omitted. To estimate the reduction in Si we use the compositions of the common intermetallic phases in Table 3. For 6061 we assume all Fe, Mn, and Cr is bound in α-AlFeMnCrSi with a (Fe+Mn+Cr):Si ratio of 4:2, resulting in a rounded loss of 0.2 mass percent Si (0.185 atom percent). For 6016 we assume almost all Fe is bound in β-AlFeSi with an Fe:Si ratio of 1:1 while Mn and Cr are bound in α-AlFeMnCrSi, leading to a rounded loss of 0.15 mass percent (0.13 atom percent).

Cooling and heating differential scanning calorimetry (DSC) measurements are carried out in a Mettler Toledo DSC 3 device using cylindrical samples with a diameter of 5 mm. The excess specific heat capacity resulting from the different precipitation and dissolution reactions is obtained using a baseline correction on the measured heat-flow curve. First, the heat flow signal of a pure Al reference sample is subtracted. Then, using the reaction-free parts of the curve at low and high temperatures as supporting points, a 3rd order polynomial fit is applied by default and subtracted whereas special attention must paid to the curvature and the critical points of the polynomial. With the exception of the interrupted cooling tests, each experiment is repeated two times with pure Al measurements in between, and the results are averaged to improve reliability. The final corrected curves are used for all further evaluations. For more details on the evaluation of DSC data, see e.g [6]. The viability and choice of the reaction-free sections require careful consideration of a wide range of DSC data and strongly depend on the alloy, the type of DSC experiment (cooling or heating) as well as the rates considered. Regarding the alloys and cooling/heating rates herein, the lower reaction-free range may be selected as, e.g., 25–150 °C. For the upper reaction-free interval in the present work, one may choose the largest possible range well above the solvus temperature of the stable phases for the cooling experiments. For the slower heating experiments shown in this work, this is also possible, albeit the width of said interval becomes smaller. For alloys with increasing Fe and Mn contents (e.g., 0.4 and 0.7 wt%), there can be a measurable contribution of dispersoid dissolution to the DSC signal in the high-temperature “reaction-free” range, appearing as an additional tilt in the baseline, so that the subtraction of a polynomial may no longer be justified [21]. For the present work, we focus only on the Al-Mg-Si-Cu phases, and the investigated alloys have substantially lower transition metal contents; hence, we assume this can be neglected. Lastly, for fast heating experiments, the definition of a reaction-free range may not be possible if the dissolution reaction extends all the way to the final temperature of the measurement.

The in-situ high-energy X-ray diffraction (HEXRD) experiments are conducted with cylindrical samples of 5 mm in diameter and 10 mm in length using the modified Baehr 805 A/D dilatometer at the high-energy materials science (HEMS) beamline P07 at PETRA III [22], which is partly operated by the Helmholtz-Zentrum Hereon. The wavelength used is 0.014235 nm with a beam cross-section of 0.5 × 0.5 mm^2; the samples are measured in transmission.

2.1. Concept

The investigations can be divided into three main parts. All samples are initially solutionized for 20 min at 560 °C. The first part consists of three continuous cooling DSC measurements at 0.0167, 0.03, and 0.167 K/s (1, 1.8, and 10 K/min). Each of these differently cooled states is then re-heated at 0.03 K/s, leading to six DSC curves per alloy. The DSC data on 6061 used in this part have been previously published by Falkinger et al [23]. The choice of cooling rates aims to include one rate where the stable precipitation reaction is prevalent (0.0167 K/s), one where the metastable reaction is prevalent (0.167 K/s), and one intermediate rate to capture the transition (0.03 K/s).

Table 1
Actual and idealized chemical compositions of alloys 6061 and 6016 in mass (atom) percent - balance is Al.

Alloy	Mg	Si	Cu	Fe	Mn	Cr
6061	0.9 (1.0)	0.7 (0.68)	0.15 (0.06)	0.45 (0.22)	0.1 (0.05)	0.2 (0.1)
6061 ideal	0.9 (1.0)	0.5 (0.48)	0.15 (0.04)	-	-	-
6016	0.35 (0.39)	1.1 (1.06)	0.1 (0.04)	0.15 (0.07)	0.1 (0.05)	0.1 (0.05)
6016 ideal	0.35 (0.39)	0.95 (0.91)	0.1 (0.04)	-	-	-

The second part includes a continuous cooling experiment at 0.167 K/s with subsequent heating at 0.05 K/s (3 K/min). The precipitate evolution is characterized with HEXRD. Complementary DSC measurements of the same samples are conducted afterward. The procedure outlined in a previous publication [8] is applied to evaluate the HEXRD data. The evolution of individual peaks, i.e., phases, is tracked as a function of time and temperature to compare them to DSC measurements and their corresponding simulations. Together with the DSC data, the present cooling and heating simulations serve as the primary consistency check for absolute values of phase fractions and the contributions of individual phases to the excess specific heat capacity. This is a key difference to reference [8], where only cooling simulations were available, and the contributions of individual phases to the heating DSC signal had to be reverse-engineered from the HEXRD data using calibrated conversion constants. In the present work, we use simulations to access the individual contributions of the precipitates to the excess specific heat for both cooling and heating experiments. The simulated derivatives of the phase fractions are then qualitatively compared to the scaled derivatives of the respective peak areas to assess if the evolution of each precipitate during cooling and heating is qualitatively correct.

Based on the first two parts, mean-field simulations are set up and optimized to best reproduce all data with only one simulation setup for each alloy.

The third part includes continuous cooling experiments on 6061 at 0.167 K/s, which are interrupted by a soaking step at 500 °C for different times. The idea is to vary the size and the fractions of different populations of β-Mg_2Si precipitates. To study the effect of the soaking time, the DSC dissolution signal during subsequent re-heating at 0.03 K/s is analyzed.

Table 2 provides an overview of the various heat treatments and samples used in the three parts of the experimental work.

2.2. Simulation setup

All simulations are performed using the thermo-kinetic software package MatCalc (version 6.05.0108, see https://www.matcalc.at). The two primary aspects of the simulations in the present work are (i) the nucleation setup (in particular, the definition of potential nucleation sites and their energy contributions), as well as (ii) the thermodynamic stability of each relevant phase.

For the nucleation step, we utilize the heterogeneous nucleation site energy descriptions developed by Miesenberger et al [24] and their distribution, as reported by Kahlenberg et al [25]. It is presently not feasible to unambiguously identify the prevalent nucleation sites and their energy benefit for each specific phase and alloy composition. For simplicity and convenience, the model is calibrated for nucleation at second-phase particles for all precipitates. The densities of different nucleation sites and their respective reduction of the nucleation barrier are adjusted based on the DSC experiments. The model parameters used are given in Appendix B. In contrast to previous publications [8,23–25], an additional precipitate population for the stable phases (β-Mg_2Si and Si) is introduced. It represents the population that nucleates at lower temperatures, i.e., at less favorable nucleation sites, but under higher chemical driving force conditions. Thermodynamic phase descriptions were slightly modified, as compared to their original assessment [26]. For a more accurate description of our experiments, we decrease the stabilities of β-Mg_2Si and β'-$Mg_{1.8}Si$. For consistency with prior enthalpy measurements and according to the thermodynamic assessment, we adapt the stability of β-Mg_2Si by changing the entropy-related term of the modeling description to 444.4*T instead of originally 440.4*T [26]. This leads to a standard molar entropy change of 1.3 J/molK. In the case of β', we change the original description −68,000+400*T to −59,200+393*T, bringing the enthalpy closer to the most recent first-principles data (12,250 J/mol [27]). These changes amount to a difference in Gibbs energy of $\Delta G^0_{Mg:Si}(\beta) = +397.5 J/(mol)$ and $\Delta G^0_{Mg:Si}(\beta') = +2396.6 J/mol$ at room temperature, respectively. Further, one binary interaction parameter for Al and Si was modified as well: $\Delta^2 L^{dis}_{Al,Si} = +800 J/mol$. These updates are implemented in the current open-licensed version of the Al-database, mc_al_v2.037.

Table 2
Overview of experimental investigations conducted and/or utilized in the present work. Initial conditions HR and CR denote hot-rolled and cold-rolled materials, respectively. Before each cooling experiment, the samples were solution heat-treated at 560 °C for 20 min (SHT).

Part	Heat treatment	6061	6016	DSC	HEXRD	Condition/Product	Reference
I	SHT+Cooling: 0.0167, 0.03, 0.167 K/s Heating to 560 °C: 0.03 K/s	Yes	Yes	Yes	No	6061: HR/Plate 6016: HR/Plate	6061: [14] 6016: present work
II	SHT+Cooling: 0.167 K/s Heating to 560 °C: 0.05 K/s	Yes	Yes	Yes	Yes	6061: HR/Plate 6016: CR/Sheet	present work present work
III	SHT+Cooling: 0.167 K/s Stop at 500 °C: 0, 27, 81 min Heating to 560 °C: 0.03 K/s	Yes	No	Yes	No	6061: HR/Plate	present work

Table 3
Phases and crystal structures used for peak identification in the present work.

Phase name	Composition	Space Group	Unit cell	References
Q/Q'	Probably $Al_3Cu_2Mg_9Si_7$	P −6	a,b = 1.039 nm c = 0.402 nm	[32,34–40]
B' or "Type-C"	probably $Al_3Mg_9Si_7$	Hexagonal	a,b = 1.04 nm c = 0.402 nm	[32,33,35,41,42]
β'	Mg_9Si_5	P 6_3/m	a,b = 0.715 nm c = 1.215 nm	[43–45]
β	Mg_2Si	F m −3 m	a = 0.639 nm	[44,46]
Si	Si	I a −3	a = 0.6636	[47]
α-AlCrFeMnSi	approx. $Al_{15}(Fe,Mn)_3Si_2$, $Al_{19}Fe_4MnSi_2$	I m −3	a = 1.253 nm	[46,48,49]
β-AlFeSi	$Al_9Fe_2Si_2$	A 2/a	a = 0,6161 nm b = 0,6175 nm c = 2,0813 nm α, γ = 90.0° β = 90.42°	[50]

3. Results

3.1. Peak assignment

To evaluate the microstructural evolution during in-situ heating from HEXRD data, the relevant phases are first identified. The crystal structures considered are found in Table 3. Then, the peaks in the diffraction patterns are assigned to the different phases in the system. This is done by using the software packages CrystalMaker [28], CrystalDiffract [29] and Highscore Plus [30]. Note that Q' typically refers to a precursor or coherent version of the Q phase [31]. Both have been reported with varying chemical compositions in the literature (see, e.g., [31]), but are structurally very similar. They are, therefore, not distinguished in the present work. The B' (or "Type-C") phase has been described as a Cu-free variation of Q/Q' with vacancies replacing Cu atoms [32], typically occurring in Cu-free excess Si alloys [33]. It is only listed for completeness, given that both alloys should contain sufficient amounts of Cu to suppress this variant in the present case.

In Figs. 1 and 2, the relevant sections of the diffractograms for 6061 and 6016 in the initial condition before solutionizing are shown. Note that the beam is not perfectly monochromatic, leading to additional peaks from the aluminum matrix at half the angle. For 6061, the peaks and identified phases correspond very well to what is expected from the literature. Regarding soluble precipitates, Q/Q', as well as β' and β-Mg_2Si are identified. For 6016, the main stable precipitate is pure Si. β-Mg_2Si and Q/Q' are also present, albeit in much lower amounts. The missing β-AlFeSi peak at roughly $2\theta = 1.57$ ° may be related to texture, that is, primary β-AlFeSi precipitates preferably aligning along certain crystal directions during rolling. Since we are predominantly interested in the soluble phases, this is of minor relevance.

For the soluble phases, texture can be an issue when evaluating peak intensities of plate or sheet products [51]. Even though the cold-rolled material typically recrystallizes during the initial solutionizing step, some preferred orientations are expected to remain for the aluminum matrix as well as the soluble phases [51]. For the present work, absolute peak areas are not required but only derivatives, i.e., changes over temperature. These are assumed to be consistent since cooling and heating are conducted in direct succession with the same sample and orientation.

4. Results for alloy 6061

4.1. 6061: DSC experiments

The experimental and simulated excess specific heat capacity during cooling of 6061 at 0.0167, 0.03, and 0.167 K/s (left to right) is shown in the upper row of Fig. 3. The bottom row shows the contributions of each specific precipitate in the simulation. The corresponding radii, phase fractions, and number densities can be found in Fig. 11 in Appendix A. Expectedly, faster cooling rates promote the formation of Q/Q' and β', whereas the stable β-Mg_2Si phase (denoted β from here on) is increasingly relevant at lower cooling rates. For the cooling simulations, the fine population of β does not play any significant role. This is a major reason why cooling simulations typically work very well using just one coarse population [23–25]. At 0.0167 and 0.167 K/s, the simulations are in excellent agreement with the experimental data. Considering that we follow a rather pragmatic way to treat nucleation by defining sets of nucleation sites with fixed number densities that more or less fully nucleate during cooling, a few deviations can be expected, for instance, for the reaction of Q/Q' between 320 and 420 °C at 0.03 K/s. This will be discussed in more detail later on.

Fig. 4 shows the influence of different cooling rates on subsequent reheating at a rate of 0.03 K/s. The corresponding radii, phase fractions, and number densities can be found in Fig. 12 in Appendix A. The sample that was previously cooled at the fastest rate of 0.167 K/s (right column) exhibits a strong growth reaction for metastable precipitates during reheating at around 300 °C. The β reaction is dominated by the fine precipitate population. The samples cooled at the slower rates of 0.03 K/s (center column), and 0.0167 K/s (left column) exhibit weaker growth of metastable precipitates. The β dissolution signal changes in shape as the coarse population increasingly contributes to the dissolution reaction.

Fig. 5 summarizes the effect of different heating rates for samples that were previously cooled at 0.03 K/s. Expectedly, the point of full solutionizing is shifted to higher temperatures as the heating rate increases from 0.0167 to 0.03 and 0.167 K/s (left, center, and right column), respectively.

The comparison of the different heating simulations in Figs. 4 and 5 with the results by Falkinger et al [23] reveals a significant improvement with regard to the simulated dissolution kinetics of the β phase. In their work [23], only a single population of β was considered without any precursors, which resulted in an overestimation of the rate-specific solvus temperature. This effect is most significant for (i) heating of quickly cooled states and (ii) fast heating processes (compare right columns in Figs. 4 and 5 with results in [23]).

It is evident that the heating simulation peaks are not quite as smooth as the experimentally measured data. In particular, the precipitation reaction of Q/Q' is slightly overestimated in some cases. However, the qualitative changes in the DSC curves are well reproduced.

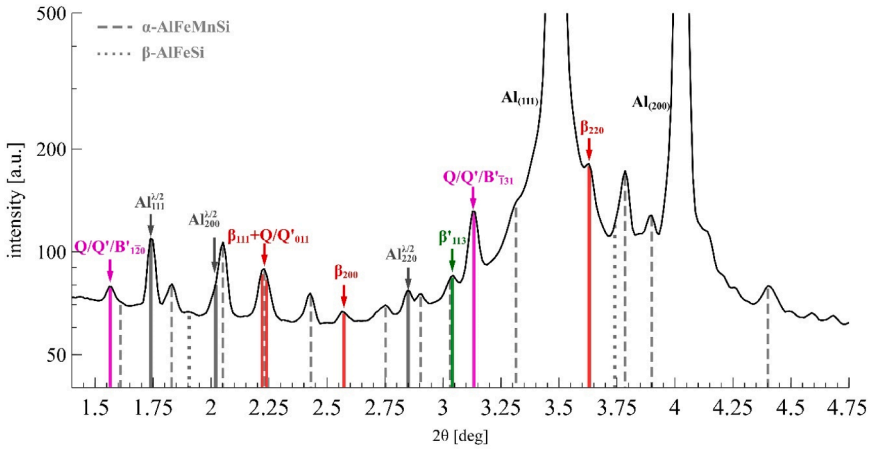

Fig. 1. Section of the diffractogram of 6061 in the initial condition before solutionizing (hot-rolled and slowly cooled). The intensity is scaled logarithmically; the peaks are assigned based on the crystal structure data in Table 3. The most relevant phases for the evaluation in the present work are Q/Q'/B', β', and β-Mg_2Si, which are highlighted in color.

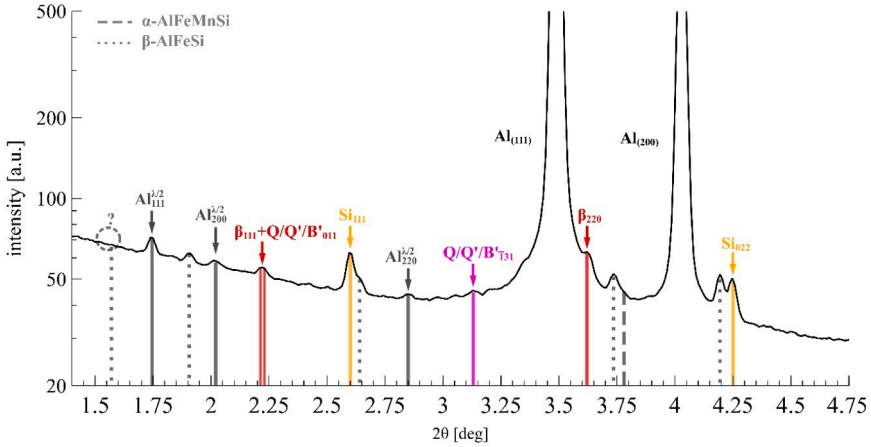

Fig. 2. Section of the diffractogram of 6016 in the initial condition before solutionizing (soft annealed and cold-rolled). The intensity is scaled logarithmically; the peaks are assigned based on the crystal structure data in Table 3. The most relevant phases for the evaluation in the present work are Q/Q', β-Mg_2Si, and pure Si, which are highlighted in color.

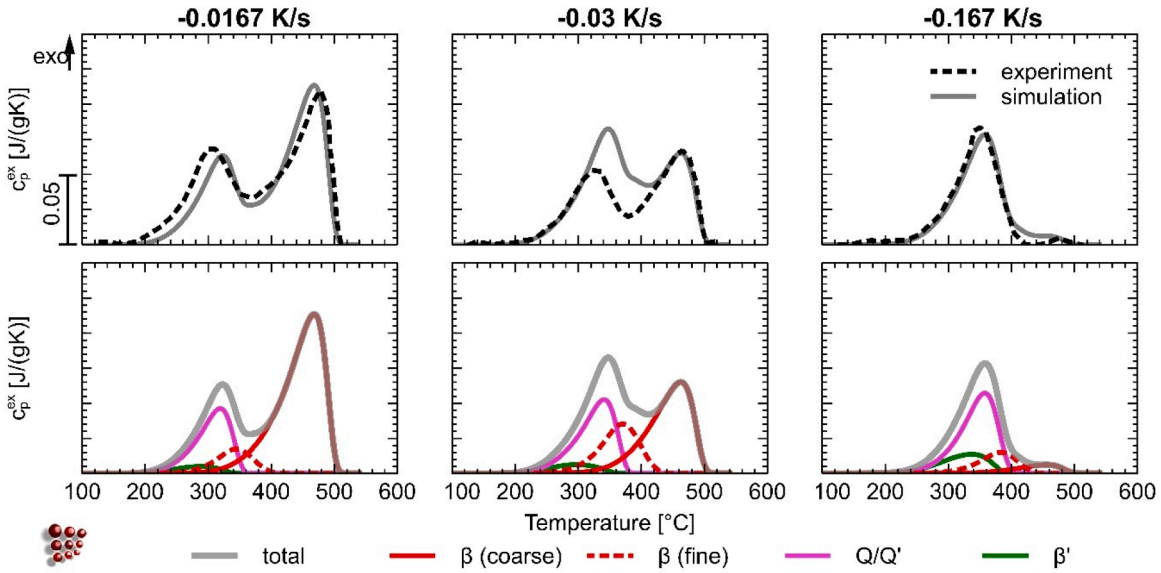

Fig. 3. Comparison of cooling DSC experiments from [23] to simulations using the setup in the present work for hot-rolled plates of 6061. The top row shows the data for the excess specific heat capacity as measured and simulated for cooling rates of 0.0167, 0.03, and 0.167 K/s (from left to right). The bottom row shows the individual contributions of all precipitates considered for the simulation. Corresponding radii, phase fractions, and number densities can be found in Fig. 11 in Appendix A.

4.2. 6061: HEXRD comparison

Fig. 6 shows the summarized results for the samples measured with both DSC and HEXRD. The DSC data are compared to the simulations for cooling at 0.167 K/s and subsequent re-heating at 0.05 K/s in the top left and right, respectively. In the lower part, the contributions to the excess specific heat of each simulated phase (colored lines) are compared to the respective scaled first derivative of the peak areas dA/dT obtained from the HEXRD experiments (colored dots/crosses).

During cooling, only a small amount of stable β seems to form, with a minor contribution to the DSC signal, apparently between 500 and 400 °C according to the DSC measurement. However, the corresponding HEXRD signal shows the β phase formation to occur continuously between 500 and 300 °C (bottom left, red dots). Upon comparison with the simulated β signal (bottom left, red line), it is clear that the addition of fine β precipitates constitutes an improvement in the quality of the simulation. The exothermic reaction between about 400 and 250 °C, predominantly related to metastable phases, is an overlap of β' and Q/Q', which are well described using a single precipitate population.

The DSC and the HEXRD data during heating are equally well reproduced with the present simulation setup. The formation reactions of β' and Q/Q' during heating are again slightly overestimated, which will be addressed in the discussion.

4.3. 6061: interrupted cooling

To explore the applicability of the present setup to discontinuous cooling strategies, a series of DSC cooling experiments from 560 °C to RT is conducted at 0.167 K/s, but the cooling process is interrupted with a soaking step at 500 °C for different time spans. The expectation is that a coarse population of β precipitates forms at this temperature, whose phase fraction and mean size increase with interruption time [6]. The samples are then re-heated at 0.03 K/s to study the effect of the interruption time on the dissolution signal of β and compare the results to the predictions of the simulations. Fig. 7 shows a detailed view of the temperature interval in which β dissolves. It is clear that with increasing

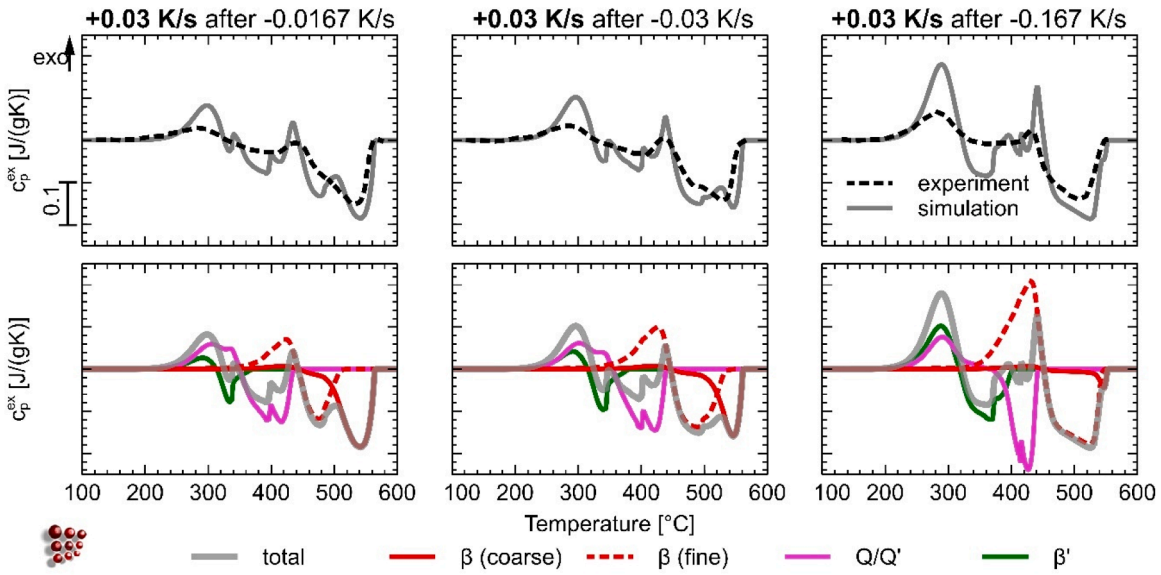

Fig. 4. Comparison of heating DSC experiments from [23] to simulations using the setup in the present work for hot-rolled plates of 6061. The top row shows the data for the excess specific heat capacity measured and simulated for heating at 0.03 K/s, starting with differently cooled states. The cooling rates for the initial conditions were 0.0167, 0.03, and 0.167 K/s (from left to right). The bottom row shows the individual contributions of all precipitates considered for the simulation. Corresponding radii, phase fractions, and number densities can be found in Fig. 12 in Appendix A.

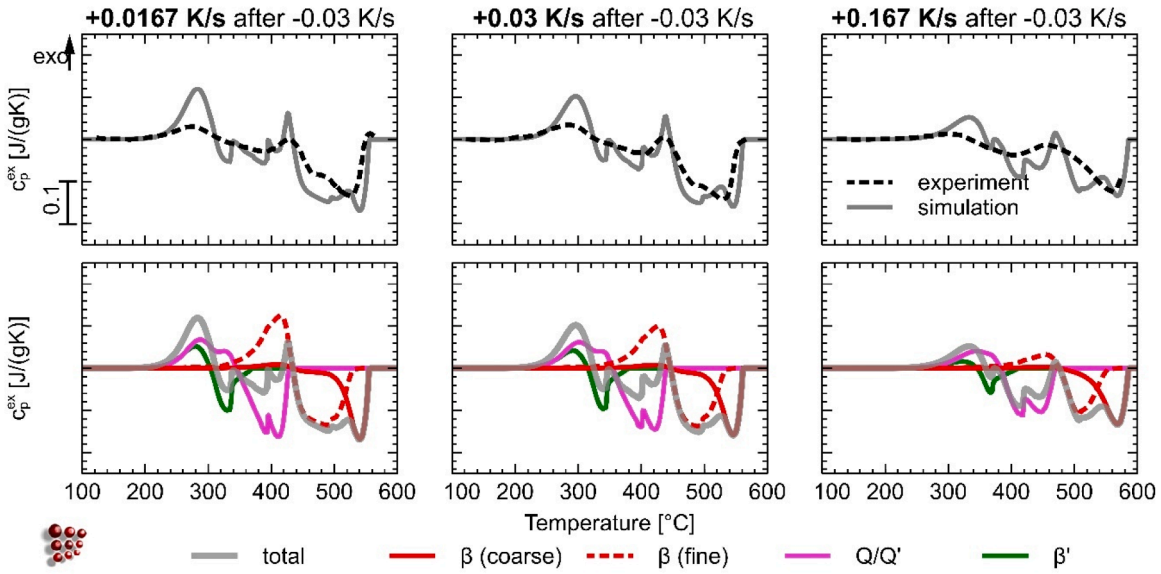

Fig. 5. Comparison of heating DSC experiments from [23] to simulations using the setup in the present work for hot-rolled plates of 6061. The top row shows the data for the excess specific heat capacity as measured and simulated for heating rates of 0.0167, 0.03, and 0.167 K/s (from left to right). The initial condition for all three experiments was cooled at 0.03 K/s. The bottom row shows the individual contributions of all precipitates considered for the simulation.

isothermal interruption times (left to right), the amount of coarse β increases, and the dissolution signal is continuously separated into two distinct peaks. At the same time, the temperature at which β is fully dissolved shifts to higher values. Both effects are well reproduced by the present simulation setup.

5. Results for alloy 6016

5.1. 6016: DSC experiments

The experimental and simulated excess specific heat capacity during cooling of 6016 at 0.0167, 0.03, and 0.167 K/s (left to right) is shown in the upper row of Fig. 8. The bottom row shows the individual contributions of each considered precipitate. The corresponding radii, phase fractions, and number densities can be found in Fig. 13 in Appendix A. Similarly to 6061, faster cooling rates lead to the precipitation of Q/Q', whereas stable Si and β dominate at lower cooling rates, in excellent agreement with experimental data.

Fig. 9 shows the influence of the initial condition on the heating DSC measurement at a rate of 0.03 K/s. The corresponding radii, phase fractions, and number densities can be found in Fig. 14 in Appendix A. Similar to 6061, the sample cooled at 0.167 K/s (right column) shows a strong growth reaction at around 300 °C. In contrast to 6061, this reaction in 6016 is mostly related to a large number of fine Si precipitates. The exothermic Q/Q' contribution occurs in the same temperature range. The samples cooled at 0.03 K/s (center column) and 0.0167 K/s (left column) exhibit a slightly weaker growth reaction of fine Si. Comparing the simulated and experimentally measured dissolution

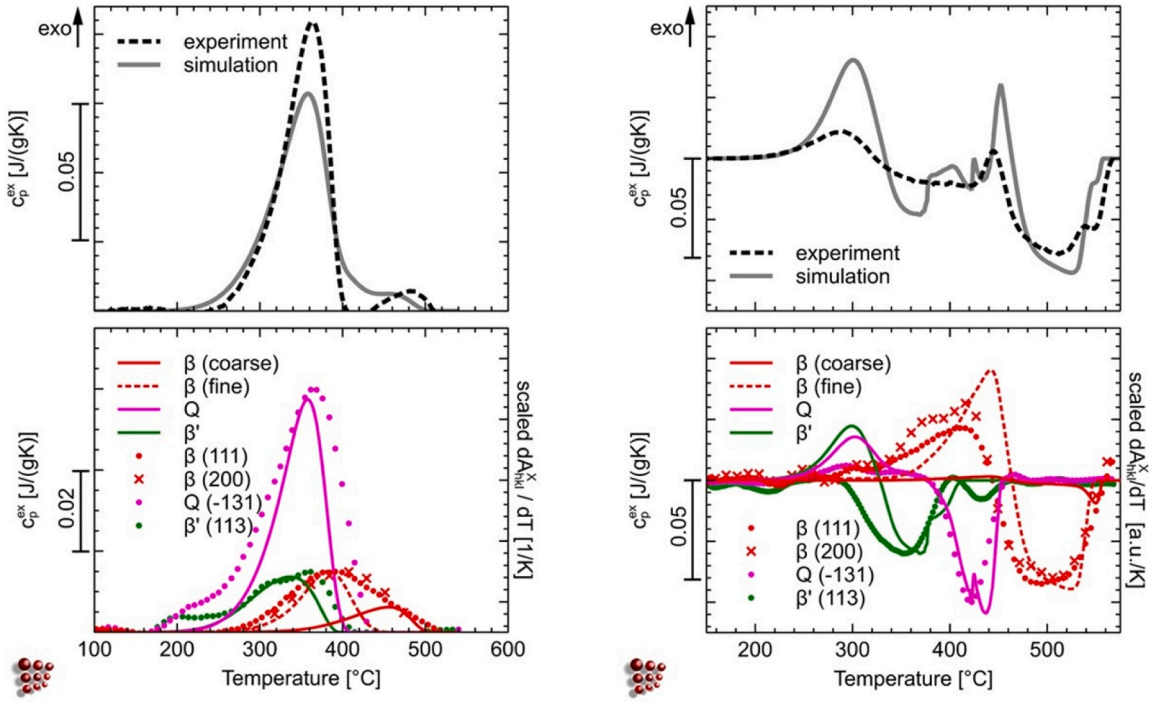

Fig. 6. Simulations, DSC and HEXRD data of 6061 during cooling at 0.167 K/s (left) and subsequent re-heating at 0.05 K/s (right). Comparison of experimental (black dotted lines) and simulated (grey lines) DSC curves are shown at the top. The simulated contributions to the excess specific heat of each precipitate (colored lines) and the scaled first derivative of the measured peak areas obtained via HEXRD (colored dots/crosses) are given below.

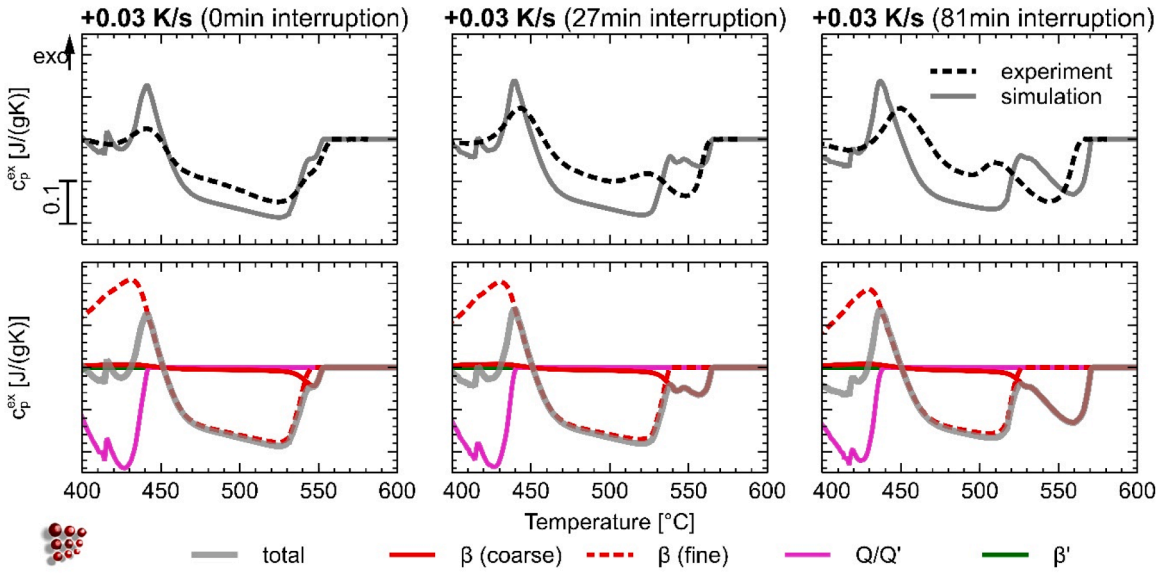

Fig. 7. Comparison of heating DSC experiments to simulations using the setup in the present work for hot-rolled plates of 6061. The shown temperature range is reduced to 400–600 °C to focus on the dissolution of β in detail. The top row shows the data for the excess specific heat capacity as measured and simulated for heating at 0.03 K/s starting with samples cooled at 0.167 K/s to room temperature with an interruption at 500 °C for different times: 0 min, 21 min, 81 min (from left to right). The bottom row shows the individual contributions of all precipitates considered for the simulation.

reactions, it is evident that the choice of two Si populations facilitates the observed spread of Si precipitates across different sizes, which is also observed in binary Al-Si alloys [12]. In comparison to 6061, only minor deviations of the simulations from the experimental DSC data are observed.

5.2. 6016: HEXRD comparison

Fig. 10 summarizes the results for the samples measured with both DSC and HEXRD for cooling at 0.167 K/s and re-heating at 0.05 K/s in the top left and right, respectively. The scaled first derivative of the peak area dA/dT for each measured phase (colored dots) and the respective contributions to the simulated excess specific heat (colored lines) are given in the bottom left and right of Fig. 10. For reasons of availability, the sample used in these experiments is taken from a cold-rolled and solutionized sheet instead of a hot-rolled and solutionized plate, resulting in a clear difference concerning the Si reaction during cooling at 0.167 K/s (compare Fig. 8 top left to Fig. 10 top left). Given that Si is

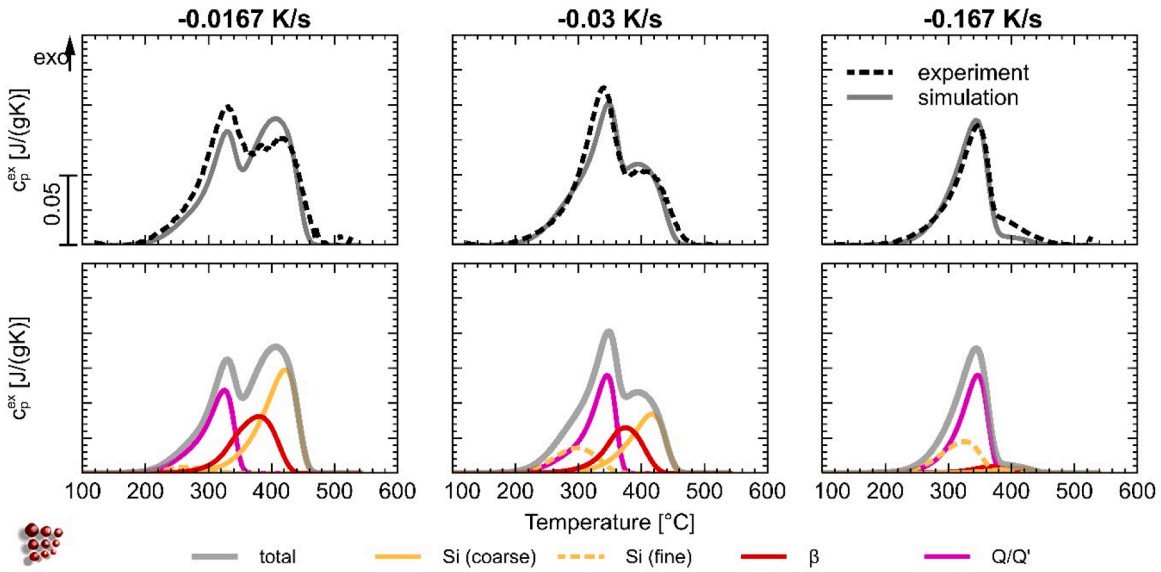

Fig. 8. Comparison of cooling DSC experiments to simulations using the setup in the present work for hot-rolled plates of 6016. The top row shows the data for the excess specific heat capacity as measured and simulated for cooling rates of 0.0167, 0.03, and 0.167 K/s (from left to right). The bottom row shows the individual contributions of all precipitates considered for the simulation. Corresponding radii, phase fractions, and number densities can be found in Fig. 13 in Appendix A.

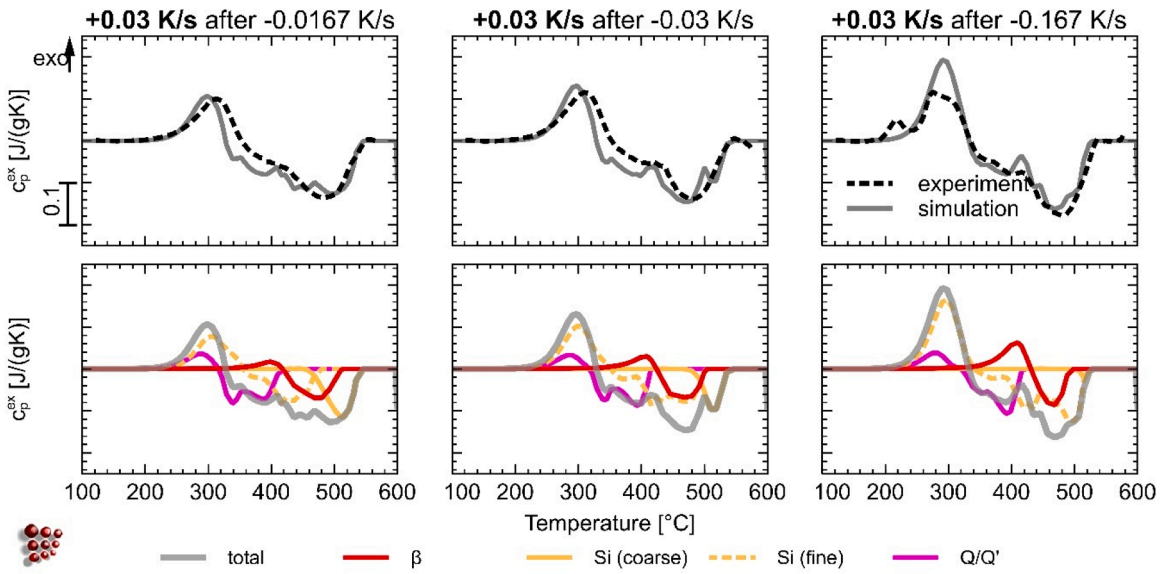

Fig. 9. Comparison of heating DSC experiments to simulations using the setup in the present work for hot-rolled plates of 6016. The top row shows the data for the excess specific heat capacity as measured and simulated for heating at 0.03 K/s, starting with differently cooled states. The cooling rates for the initial conditions were 0.0167, 0.03, and 0.167 K/s (from left to right). The bottom row shows the individual contributions of all precipitates considered for the simulation. Corresponding radii, phase fractions, and number densities can be found in Fig. 14 in Appendix A.

known to nucleate at grain boundaries where it grows at an accelerated rate [14] and the grain structures of these two materials should be substantially different, this discrepancy is plausible. Note that the difference is not nearly as clear in the DSC signal during heating at 0.05 K/s, but only shows up when comparing the simulation with the HEXRD signal (Fig. 10, bottom right). Apart from the additional Si precipitation during cooling, the simulations agree well with the DSC and HEXRD data. The β phase is only shown for the heating experiment, as there was no measurable HEXRD signal during cooling due to the negligibly small phase fraction.

6. Discussion

6.1. Smoothness of simulated and experimental DSC curves

Firstly, it is important to realize that Numerical Kampmann-Wagner (NKW) approaches based on CALPHAD databases, such as the one used in the present work, usually assume identical nucleation and growth/dissolution conditions for each precipitate population. Precipitates of one phase are assumed to have identical nucleation conditions and chemistry, and the surrounding matrix composition is also the same for every precipitate. This certainly oversimplifies the real microstructure in which off-stoichiometric precipitates, as well as other heterogeneities, affect the local chemical and diffusional environment. Spatial differences may include, for instance, segregation and localized changes in

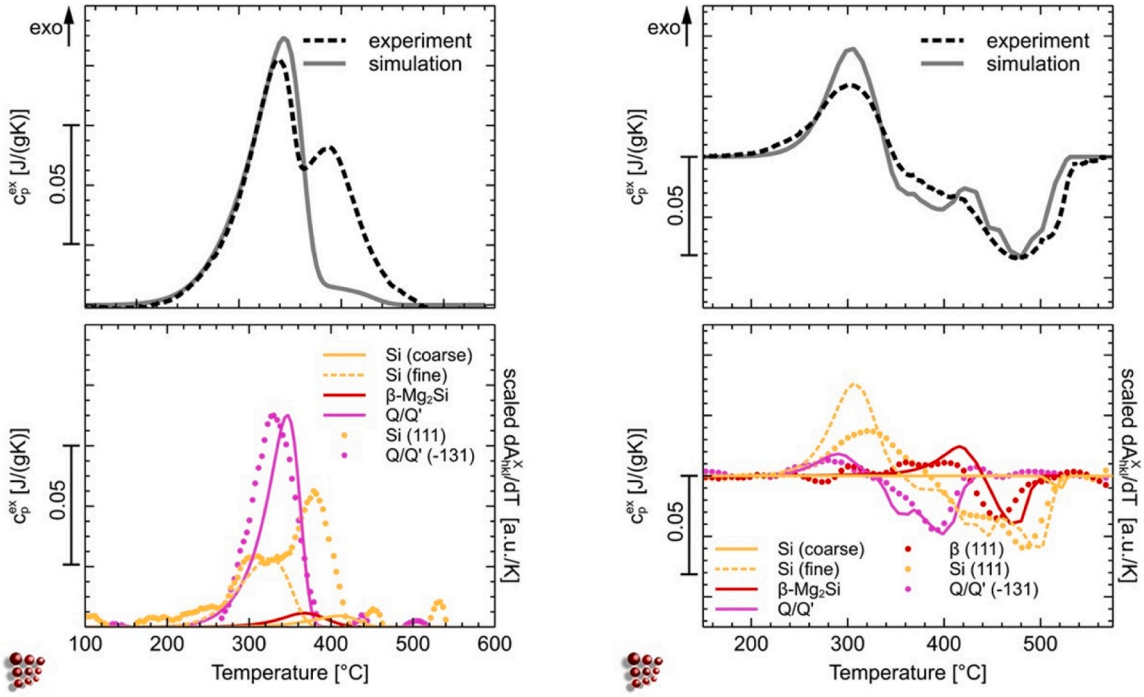

Fig. 10. Simulations, DSC and HEXRD data of 6016 during cooling at 0.167 K/s (left) and subsequent re-heating at 0.05 K/s (right). Comparison of experimental (black dotted lines) and simulated (grey lines) DSC curves are shown at the top. The simulated contributions to the excess specific heat of each precipitate (colored lines) and the scaled first derivative of the measured peak areas obtained via HEXRD (colored dots) are given below.

defect densities (e.g., grain boundaries or 2nd phase particles). We argue that the combination of these variations eventually leads to a much smoother DSC signal in experiments.

Concerning variations in the nucleation behavior, the previously published distribution of heterogeneous nucleation site energies [25] that is also used in the present work offers some correction, especially for cooling simulations. Details on the nucleation setup will be discussed in the next chapter.

However, it is apparent that the simulated dissolution reactions during heating still tend to be sharper than the experimental data in some cases (see Fig. 4, Fig. 5) - the same effect has also been observed in earlier works [26,52]. Considering the aforementioned points, the reduced smoothness should be most pronounced for metastable phases with broad composition ranges, for which alloy-dependent thermodynamics and compositions are more challenging to assess. Fittingly, the differences between simulations and experiment are largest in the lower temperature range (see Fig. 4, Fig. 5), where β' and Q/Q' are prevalent. Especially the Q/Q' phase and its Cu-free variation B' (or "Type C") are good examples for phases that are challenging to assess and which may contribute to the difficulties we encounter when calibrating the simulation setup. Conversely, stochiometric and stable precipitates such as Si and β are significantly easier to assess thermodynamically, and consequently, their dissolution behavior is comparably less complicated to model.

Overall, the evolution of individual phases in the simulations of the present work agrees very well with the HEXRD data. Additionally, the relevant trends in the DSC signal regarding the dissolution behavior of stable precipitates are reproduced, highlighting the potential of the approach outlined herein.

6.2. *Nucleation setup*

From the viewpoint of simulations, getting stable precipitates to nucleate at the correct temperature within the framework of CNT requires a reduction in the classical nucleation barrier (volume and surface contributions), either by lowering the interface energy and/or considering the energy gain at various heterogeneous nucleation sites. The latter concept has been successfully worked out in the recent work by Miesenberger et al [24]. Still, absolute values within rigorous models for these contributions are difficult to assess, and practical mean values are used instead.

The present work estimates the total number density of heterogeneous nucleation sites based on DSC data without any detailed assumption about the type of site. It proposes a simple and pragmatic approach to model nucleation during cooling and heating at moderate rates by including two precipitate populations of the stable phase.

The results suggest that the combination of mean-field simulations, HEXRD, and DSC constitutes a promising strategy to improve nucleation models and thermodynamic descriptions in the foreseeable future. This includes isolating the influence of individual microstructural features on

specific phases, such as the effect of grain size on the nucleation and growth of Si. Another example would be the evaluation of different definitions of the nucleation site density. For instance, for nucleation at dispersoids, one may define (i) one nucleation site per dispersoid or (ii) one site per surface atom of each dispersoid. Naturally, this definition will affect how the remaining setup must be calibrated. We note that the defined nucleation sites in the present work tend to be on the lower end regarding the site density, with a correspondingly stronger reduction of the nucleation barrier. This leads to an almost full saturation of nucleation sites during cooling in all cases. For moderate cooling and heating treatments such as the ones considered in the present work, this should be a fair assumption given that the HEXRD data for the fastest cooling rate, 0.167 K/s, still shows a substantial precipitation reaction of the stable phases for both alloys (see Figs. 6 and 10), and the subsequent heating signals are well reproduced. However, the low nucleation barriers required to trigger nucleation at heterogeneous sites for very small undercoolings also lead to high site saturations at significantly faster cooling rates (e.g. 50 K/s, not shown). While the limited diffusion adequately suppresses any noticeable reaction in the simulated DSC signal for these cases, the low sensitivity of the site saturation to the cooling rate in the present approach will need further investigation. It is presently not clear to what extent nucleation actually commences during cooling and/or re-heating for arbitrary cooling and heating rates, and addressing this issue experimentally and/or computationally is beyond the scope of the present work. From an experimental point of view, it is difficult to verify, for instance, the existence of nuclei with number densities of 1e14/m^3. From a computational point of view, this aspect quickly leads to some well-known and profound questions regarding the capability of CNT to predict solid-state nucleation [53], especially for non-isothermal treatments. As of now, for most mean-field models, including the present work, a substantial amount of calibration is required, and usually a high sensitivity to small changes in certain input parameters or alloy composition remains. This means that in their present form, the setups are alloy specific, and the accuracy of predictions for varying dispersoid densities (mostly related to the transition metal content) and general changes in composition is limited.

At the same time, we note that there are a few effects that may be worth taking into account for improved mean-field approaches in the future. For instance, in a recent work by Hutchinson and Bréchet [54], an alternative approach to solid-state nucleation based on geometric clusters resulted in an improved description of nucleation for kinetically constrained systems. Furthermore, non-classical effects such as coalescence of subcritical clusters can facilitate overcoming the nucleation barrier and may deserve further consideration [55]. It remains to be seen under which exact conditions these approaches improve mean-field simulations for cases such as the one considered in the present work.

6.3. Alloy 6061

The relation between the precipitate radius and the dissolution time of precipitates in general [56], and β in particular [57], is well-investigated. The nature of the comparably broad dissolution reaction of β in DSC measurements relating to the existence of multiple populations of β precipitates has also been mentioned a few times in the literature [7,58]. However, no study has yet addressed the separation of β dissolution reactions in DSC measurements in such detail and provided an experimentally verified simulation framework to reproduce this effect. Overall, the results for 6061 in the pragmatic approach of the present work look promising. Nevertheless, a few uncertainties remain. The most fundamental open questions in the simulations relate to the choice of potential nucleation sites and the calculation of nucleation barriers that were mentioned in the previous chapter.

During the cooling experiments (comparably straightforward, as just precipitation occurs), different approaches regarding the nucleation setup can be taken. For instance, β, as well as the Q/Q'-Phase and other metastable precipitates in technical alloys, preferably nucleate at large intermetallics and dispersoids (see [5–11]) whose number densities and/or estimated number of surface atoms may be considered as an input value for the nucleation site density. Interestingly, such pre-existing second-phase particles of any kind do not seem to be a necessity for the nucleation of β during cooling, as it readily precipitates in pure alloys as well [5,6]. This was recently investigated in a study by Hennum et al [5], who compared pure and technical alloys and discussed the effect on the precipitation of β. They conclude that the reaction is not limited by nucleation but rather by bulk diffusion and argue that pure ternary Al-Mg-Si alloys probably still contain sufficient defects (subgrain boundaries, dislocations, etc.) to fully precipitate β. However, it remains unclear which defects contribute to what extent.

In contrast, metastable phases (the low-temperature reactions) are significantly affected by the presence of dispersoids, resulting in a measurable difference between pure and industrial alloys [6]. In principle, more dispersoids (nucleation sites) also lead to more metastable precipitates in the present framework. However, further investigations are required to, e.g., properly assess the nucleation sites in such a way that the simulated DSC signal of metastable precipitates reacts adequately to changes in the dispersoid density and achieve a smooth transition to pure alloying systems without any dispersoids.

With respect to the heating simulations, it remains uncertain to what extent secondary nucleation mechanisms at precursors during heating or any transformation reactions into stable phases require consideration. For some alloys, such as 6082 [8] and 6061 (herein), it is certain that the formation reaction of β during heating overlaps with the dissolution of the precursor precipitates (B' or Q/Q'). Previous in-situ TEM studies by some of the present authors [7] suggested that the formation of β during heating in 6061 involves nucleation at dispersoids and metastable precursors, followed by a "precipitate-related transformation". The model in the present study on moderate cooling and heating rates works based on the assumption that a population of small β already exists after cooling to room temperature. In the simulations, the bulk diffusion turns out to be sufficient to qualitatively reproduce the aforementioned overlap of the dissolution of Q/Q' with the growth of β, even though their pre-defined number densities vary by two orders of magnitude. Hence, in line with the arguments of Hennum et al [5], it may not be necessary to consider any direct or indirect transformation mechanisms – at least not for the growth of β. It is also interesting to note that the dissolution signal during re-heating of β after cooling at 0.167 K/s is fairly similar to those observed for heating from an as-quenched state or T6 condition. In spite of the remaining questions regarding a universal nucleation setup for fully arbitrary heat treatments, the present approach is capable of capturing key aspects concerning the dissolution behavior of stable β surprisingly well.

6.4. Alloy 6016

The simulated temperatures/times at which Si is fully dissolved agree very well with the DSC experiments, which is the main prerequisite for reliable simulations of, e.g., solutionizing treatments. The same is true for the evolution of metastable precipitates. In contrast to

6061, the low-temperature reaction (250–400 °C) of 6016 does not include any measurable amounts of β‘, and it is well described with nucleation and growth of only Q/Q’ and fine Si. In accordance with the literature, Si precipitation seems to be significantly affected by the defect microstructure and, in particular, by the grain size [14]. However, a proper assessment of this effect would require additional experiments to compare microstructural states with systematically varying grain sizes, which is beyond the scope of the concept outlined in the present work.

Finally, we emphasize that fine Si does not strongly contribute to the DSC signal during cooling and would not have been considered without the HEXRD data and the heating experiments, underlining the advantage of combining different methods.

7. Conclusion

The present work provides an experimentally verified, simple setup for thermo-kinetic simulations that can be used to estimate the time required for full solutionizing based on a given precondition, e.g. a certain cooling strategy after homogenization and/or intermediate annealing steps for the two alloys EN AW-6061 and EN AW-6016. The setup accurately describes precipitation and dissolution during heating as well as cooling for the later stages of the precipitation sequence over a wide range of cooling/heating rates, with one parameter set for each alloy. The proposed methodology constitutes a significant improvement over previously published approaches of a similar kind [8,23]. The following key points are concluded:

- ➔ To simulate the high-temperature reaction in DSC cooling experiments of 6061 and 6016, one population of the respective stable phase (β-Mg_2Si or Si) nucleating at energetically favorable sites is sufficient.
- ➔ The HEXRD data reveal that stable precipitates (β-Mg_2Si or Si) also form at lower temperatures, but these have only limited contributions to the cooling DSC signal and are easily missed due to overlaps with other precipitation reactions.
- ➔ For simulations of heating DSC experiments after cooling at moderate rates, the formation of stable precipitates at lower temperatures has to be considered as well. This can be done, e.g., in the form of an additional precipitate population nucleating at less favorable sites, with a higher number density.
- ➔ Some precipitates appear to be more influenced by microstructural features (presence of dispersoids, grain structure, etc.) than others. Metastable precipitates and Si seem especially sensitive to variations in defect densities.
- ➔ The NKW setup herein captures the contribution of phases from the later precipitation stages to the excess specific heat, the transformation rates, and their kinetic dependencies within the investigated range of cooling and heating rates.

The proposed combination of DSC, HEXRD, and mean-field simulations facilitates more sophisticated simulations in the future. For instance, by (i) extracting the influence of certain microstructural features on individual phases, thus (ii) allowing a comparison between different setups to get more reliable descriptions for nucleation, and (iii) overall improving thermodynamic descriptions of metastable and stable precipitates.

CRediT authorship contribution statement

Robert Kahlenberg: Writing – review & editing, Writing – original draft, Software, Project administration, Methodology, Investigation, Formal analysis, Conceptualization. **Georg Falkinger:** Writing – original draft, Resources, Project administration, Investigation, Funding acquisition, Formal analysis, Conceptualization. **Roman Schuster:** Writing – original draft, Supervision, Investigation. **Bernhard Miesenberger:** Investigation. **Nicolás García Arango:** Writing – original draft, Investigation. **Emad Maawad:** Investigation. **Erwin Povoden-Karadeniz:** Writing – original draft, Data curation. **Benjamin Milkereit:** Writing – original draft, Supervision. **Ernst Kozeschnik:** Writing – original draft, Supervision, Project administration, Funding acquisition.

Declaration of competing interest

The authors declare that they have no known competing financial interests or personal relationships that could have appeared to influence the work reported in this paper.

Robert Kahlenberg
Georg Falkinger
Roman Schuster
Bernhard Miesenberger
Nicolás García Arango
Emad Maawad
Erwin Povoden-Karadeniz
Benjamin Milkereit
Ernst Kozeschnik

Acknowledgments

The authors gratefully acknowledge the financial support under the scope of the COMET program within the K2 Center “Integrated Computational Material, Process and Product Engineering (IC-MPPE)” (Project 886385). This program is supported by the Austrian Federal Ministries for Economy, Energy and Tourism (BMWET) and for Innovation, Mobility and Infrastructure (BMIM), represented by the Austrian research funding association (FFG), and the federal states of Styria, Upper Austria and Tyrol.

We acknowledge DESY (Hamburg, Germany), a member of the Helmholtz Association HGF, for the provision of experimental facilities. Parts of this research were carried out at PETRA III and we would like to thank the Hereon staff for assistance in using the high energy materials science (HEMS) beamline P07. Beamtime was allocated for Proposal I-20220550 EC.

The authors further acknowledge TU Wien Bibliothek for financial support through its Open Access Funding Programme.

Appendix A

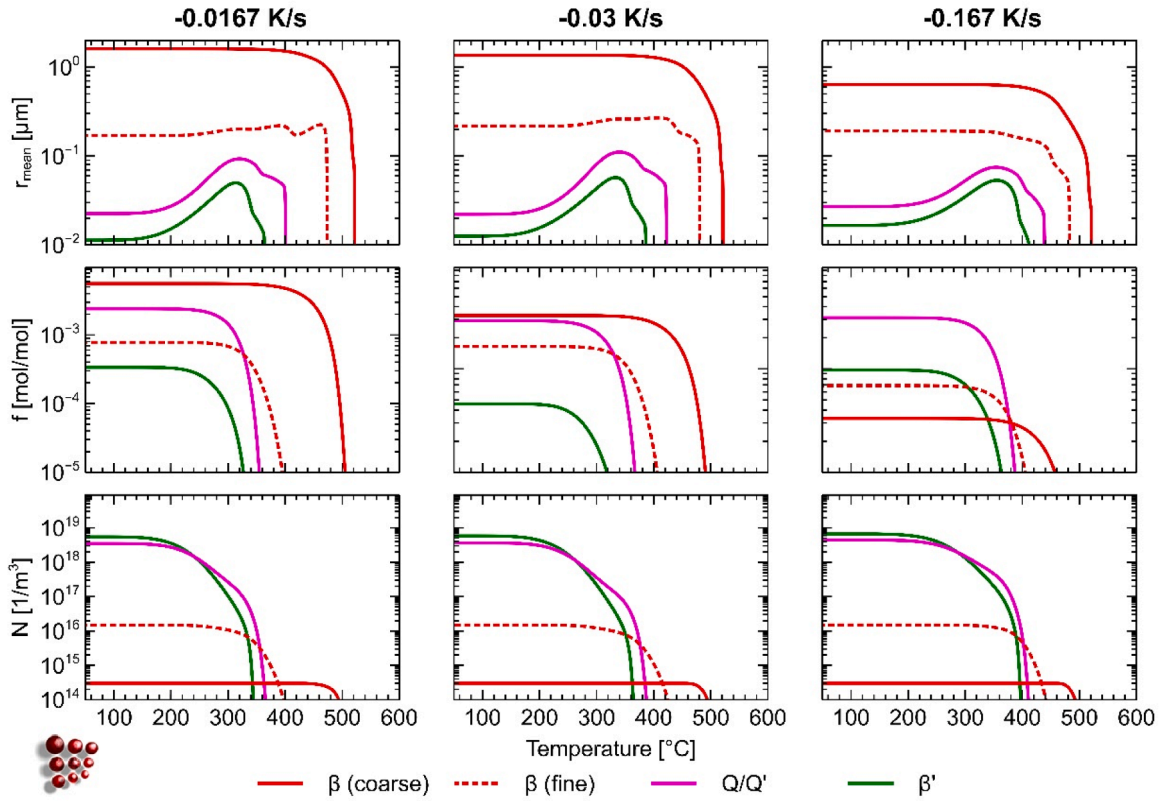

Fig. 11. Overview of mean radii r, phase fractions f and precipitate number densities N during cooling at −0.0167, −0.03 and −0.167 K/s (from left to right) using the setup in the present work for hot rolled plates of 6061.

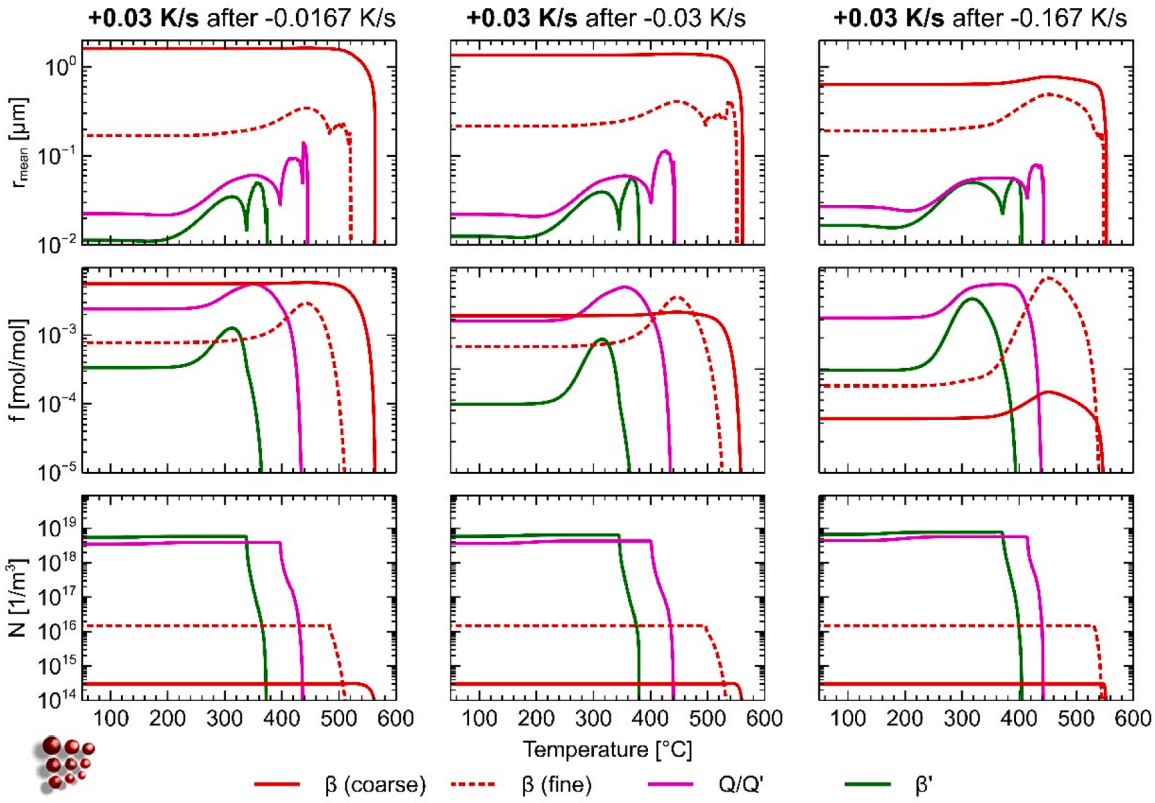

Fig. 12. Overview of mean radii r, phase fractions f and precipitate number densities N during heating at 0.03 K/s, starting with differently cooled states using the setup in the present work for hot rolled plates of 6061. The cooling rates for the initial conditions were −0.0167, −0.03, and −0.167 K/s (from left to right).

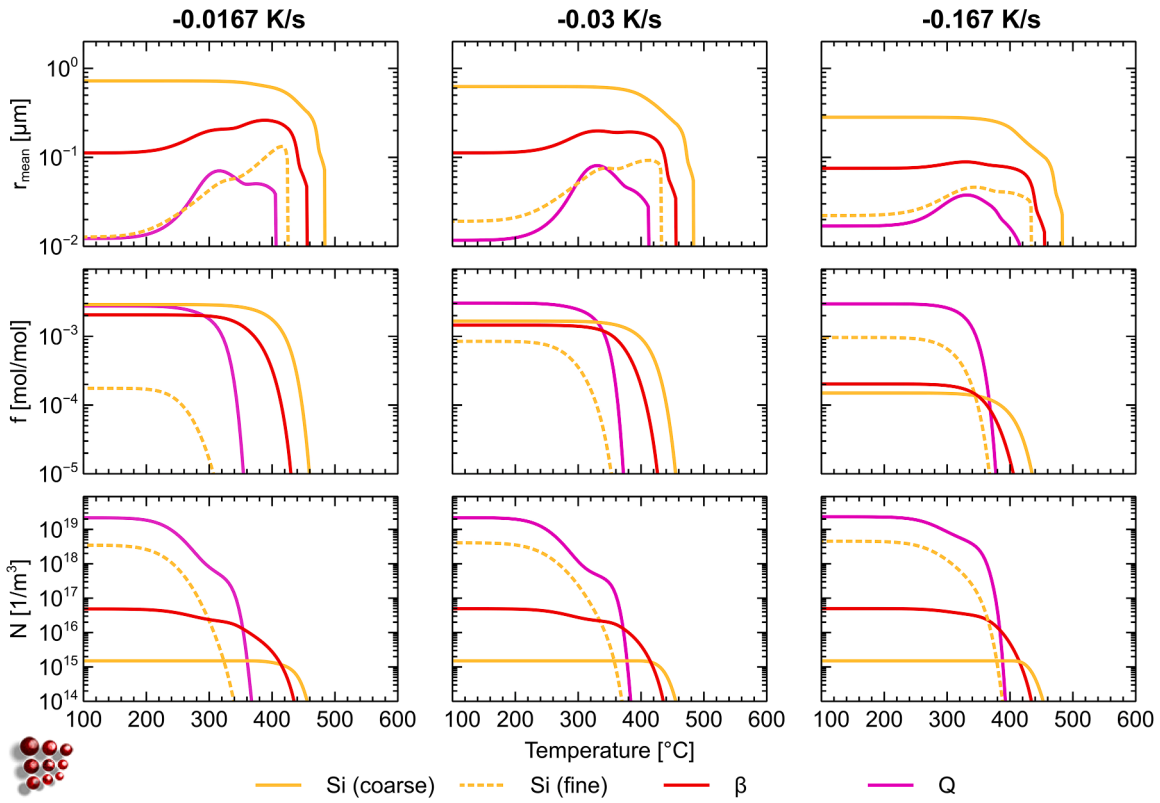

Fig. 13. Overview of mean radii r, phase fractions f and precipitate number densities N during cooling at −0.0167, −0.03 and −0.167 K/s (from left to right) using the setup in the present work for hot rolled plates of 6016.

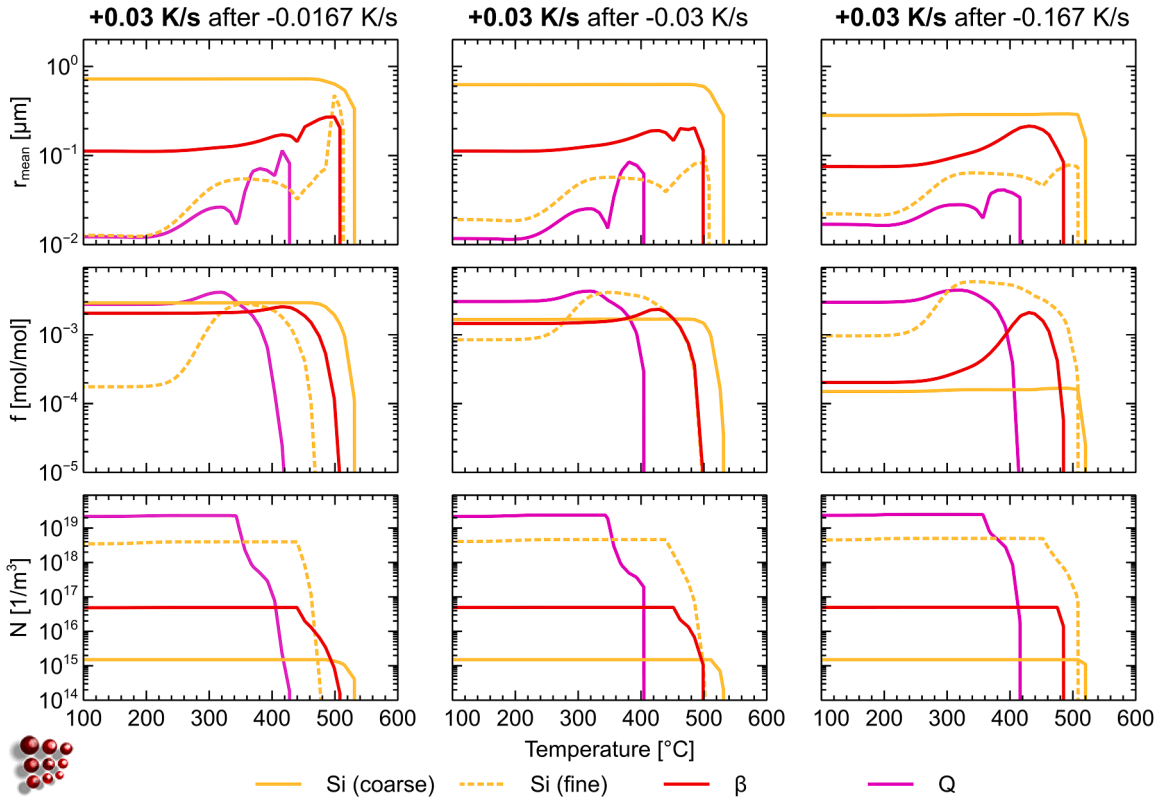

Fig. 14. Overview of mean radii r, phase fractions f and precipitate number densities N during heating at 0.03 K/s, starting with differently cooled states using the setup in the present work for hot rolled plates of 6016. The cooling rates for the initial conditions were −0.0167, −0.03, and −0.167 K/s (from left to right).

Appendix B

Nucleation model parameters used in the present work.

Parameter	EN AW-6061	EN AW-6016
T_{crit} for β'-Mg_9Si_5	2200 K [59]	-
T_{crit} for Q- $Al_3Cu_2Mg_9Si_7$	1500 K	1500 K
T_{crit} for β-Mg_2Si	1950 K [59]	1950 K [59]
T_{crit} for Si	-	1800 K
Site boundary energy γ_{GB}	0.5 Jm^{-2}	0.5 Jm^{-2}
Heterogeneous interface energy factors κ_i / κ_s (for model details see [24])		
β'-Mg_9Si_5	0.75 / 0.25	-
Q- $Al_3Cu_2Mg_9Si_7$	0.85 / 0.15	0.725/0.15
Coarse β-Mg_2Si	0.6 / 0.55	-
Fine β-Mg_2Si	0.75 / 0.25	0.7/0.3
Coarse Si	-	0.6/0.35
Fine Si	-	0.75/0.15
Distribution parameters d / n (for model details see [25])		
β'-Mg_9Si_5	0.6/0.9	-
Q- $Al_3Cu_2Mg_9Si_7$	0.5/1.0	0.25/1.0
Coarse β-Mg_2Si	0.3/1.25	-
Fine β-Mg_2Si	0.6/1.25	0.6/1.0
Coarse Si	-	0.3/1.0
Fine Si	-	0.2/1.0
Total number density of nucleation sites		
β'-Mg_9Si_5	$8{\cdot}10^{18}$ m^{-3}	-
Q- $Al_3Cu_2Mg_9Si_7$	$6{\cdot}10^{18}$ m^{-3}	$2.5{\cdot}10^{19}$ m^{-3}
Coarse β-Mg_2Si	$3{\cdot}10^{14}$ m^{-3}	-
Fine β-Mg_2Si	$1.5{\cdot}10^{16}$ m^{-3}	$5{\cdot}10^{16}$ m^{-3}
Coarse Si	-	$1.5{\cdot}10^{15}$ m^{-3}
Fine Si	-	$5{\cdot}10^{18}$ m^{-3}

Data availability

Data will be made available on request.

References

[1] C.D. Marioara, et al., Atomic structure of clusters and GP-zones in an Al-Mg-Si alloy, Acta Mater. 269 (May 2024) 119811, https://doi.org/10.1016/j.actamat.2024.119811.

[2] X. Chen, et al., Investigation of vacancy trapping by solutes during quenching in aluminum alloys, Acta Mater. 254 (Aug. 2023) 118969, https://doi.org/10.1016/j.actamat.2023.118969.

[3] L. Ding, et al., On the order–disorder transformation within a main hardening precipitate in Al–Mg–Si alloys, Philos. Mag. 105 (3) (Feb. 2025) 169–188, https://doi.org/10.1080/14786435.2024.2415290.

[4] P. Aster, et al., Unraveling the potential of Cu addition and cluster hardening in Al-Mg-Si alloys, Materials 36 (Aug. 2024) 102188, https://doi.org/10.1016/j.mtla.2024.102188.

[5] E. Hennum, K. Marthinsen, U.H. Tundal, Effect of microstructure on the precipitation of β-Mg2Si during cooling after homogenisation of Al-Mg-Si alloys, Metals 14 (2) (Feb. 2024) 215, https://doi.org/10.3390/met14020215.

[6] B. Milkereit, M.J. Starink, P.A. Rometsch, C. Schick, O. Kessler, Review of the quench sensitivity of aluminium alloys: analysis of the kinetics and nature of quench-induced precipitation, Materials 12 (24) (Dec. 2019) 4083, https://doi.org/10.3390/ma12244083.

[7] R. Kahlenberg, T. Wojcik, G. Falkinger, A. Krejci, B. Milkereit, E. Kozeschnik, On the precipitation mechanisms of β-Mg2Si during continuous heating of AA6061, Acta Mater. (Sep. 2023) 119345, https://doi.org/10.1016/j.actamat.2023.119345.

[8] R. Kahlenberg, et al., Revisiting high-energy X-ray diffraction and differential scanning calorimetry data of EN AW-6082 with mean field simulations, Thermochim. Acta 740 (Oct. 2024) 179848, https://doi.org/10.1016/j.tca.2024.179848.

[9] O. Lohne, Quench sensitivity in aluminum-magnesium-silicon alloys containing manganese or chromium, Scand. J. Metall. 12 (1) (1983).

[10] K. Strobel, et al., Quench sensitivity in a dispersoid-containing Al-Mg-Si alloy, Metall. Mater. Trans. A 50 (4) (Apr. 2019) 1957–1969, https://doi.org/10.1007/s11661-019-05130-2.

[11] K. Strobel, M.A. Easton, L. Sweet, M.J. Couper, J.-F. Nie, Relating quench sensitivity to microstructure in 6000 series aluminium alloys, Mater Trans. 52 (5) (2011) 914–919, https://doi.org/10.2320/matertrans.L-MZ201111.

[12] P. Schumacher, S. Pogatscher, M.J. Starink, C. Schick, V. Mohles, B. Milkereit, Quench-induced precipitates in Al–Si alloys: calorimetric determination of solute content and characterisation of microstructure, Thermochim. Acta 602 (Feb. 2015) 63–73, https://doi.org/10.1016/j.tca.2014.12.023.

[13] P. Schumacher, Plastisches Verformungsverhalten unterkühlter Aluminiumlegierungen im System Al-Mg-Si, Universität Rostock, 2018. PhD Thesis.

[14] G. Falkinger, R. Kahlenberg, M. Theissing, S. Mitsche, A. Thum, S. Pogatscher, Modeling the concurrent growth of inter- and intragranular Si precipitates during slow cooling of the alloy AA6016, Eur. J. Mater. 4 (1) (Mar. 2024), https://doi.org/10.1080/26889277.2024.2316914.

[15] H.S. Rosenbaum, D. Turnbull, On the precipitation of silicon out of a supersaturated aluminum-silicon solid solution, Acta Metall. 6 (10) (Oct. 1958) 653–659, https://doi.org/10.1016/0001-6160(58)90160-3.

[16] M. Liu, H. Fu, L. Tian, W. Xiao, Q. Peng, C. Ma, Nucleation and growth mechanisms of nano-scaled Si precipitates in Al-7Si supersaturated solid solution, Mater. Des. 121 (May 2017) 373–382, https://doi.org/10.1016/j.matdes.2017.02.082.

[17] E. Kozeschnik, Mean-field microstructure kinetics modeling. Encyclopedia of Materials: Metals and Alloys, Elsevier, 2022, pp. 521–526, https://doi.org/10.1016/B978-0-12-819726-4.00055-7.

[18] "TC-PRISMA: Thermodynamic and diffusion calculations." [Online]. Available: https://thermocalc.com/products/add-on-modules/precipitation-module-tc-prisma/.

[19] W. Cao, et al., PANDAT software with PanEngine, PanOptimizer and PanPrecipitation for multi-component phase diagram calculation and materials property simulation, CALPHAD. 33 (2) (Jun. 2009) 328–342, https://doi.org/10.1016/j.calphad.2008.08.004.

[20] Q. Du, K. Tang, C.D. Marioara, S.J. Andersen, B. Holmedal, R. Holmestad, Modeling over-ageing in Al-Mg-Si alloys by a multi-phase CALPHAD-coupled Kampmann-Wagner numerical model, Acta Mater. 122 (Jan. 2017) 178–186, https://doi.org/10.1016/j.actamat.2016.09.052.

[21] R.H. Kemsies, B. Milkereit, S. Wenner, R. Holmestad, O. Kessler, In situ DSC investigation into the kinetics and microstructure of dispersoid formation in Al-Mn-Fe-Si(-Mg) alloys, Mater. Des. 146 (May 2018) 96–107, https://doi.org/10.1016/j.matdes.2018.03.007.

[22] N. Schell, A. King, F. Beckmann, T. Fischer, M. Müller, A. Schreyer, The high energy materials science beamline (HEMS) at PETRA III, Mater. Sci. Forum. 772 (Nov. 2013) 57–61, https://doi.org/10.4028/www.scientific.net/MSF.772.57.

[23] G. Falkinger, C. Reisecker, S. Mitsche, Analysis of the evolution of Mg 2 Si precipitates during continuous cooling and subsequent re-heating of a 6061 aluminum alloy with differential scanning calorimetry and a simple model, Int. J. Mater. Res. 113 (4) (Apr. 2022) 316–326, https://doi.org/10.1515/ijmr-2021-8443.

[24] B. Miesenberger, E. Kozeschnik, B. Milkereit, P. Warczok, E. Povoden-Karadeniz, Computational analysis of heterogeneous nucleation and precipitation in AA6005 Al-alloy during continuous cooling DSC experiments, Materials 25 (Sep. 2022) 101538, https://doi.org/10.1016/j.mtla.2022.101538.

[25] R. Kahlenberg, G. Falkinger, B. Milkereit, E. Kozeschnik, Modeling of heterogeneous site energy distributions in precipitate nucleation, Model. Simul. Mat. Sci. Eng. 31 (8) (Dec. 2023) 085003, https://doi.org/10.1088/1361-651X/acf512.

[26] E. Povoden-Karadeniz, P. Lang, P. Warczok, A. Falahati, W. Jun, E. Kozeschnik, CALPHAD modeling of metastable phases in the Al–Mg–Si system, CALPHAD. 43 (Dec. 2013) 94–104, https://doi.org/10.1016/j.calphad.2013.03.004.
[27] B. Zhang, L. Wu, B. Wan, J. Zhang, Z. Li, H. Gou, Structural evolution, mechanical properties, and electronic structure of Al–Mg–Si compounds from first principles, J. Mater. Sci. 50 (19) (Oct. 2015) 6498–6509, https://doi.org/10.1007/s10853-015-9209-4.
[28] "CrystalMaker®: a crystal and molecular structures program for Mac and Windows." [Online]. Available: www.crystalmaker.com.
[29] "CrystalDiffract®: a powder diffraction program for Mac and Windows." [Online]. Available: www.crystalmaker.com.
[30] T. Degen, M. Sadki, E. Bron, U. König, G. Nénert, The HighScore suite, Powder. Diffr. 29 (S2) (Dec. 2014) S13–S18, https://doi.org/10.1017/S0885715614000840.
[31] D.J. Chakrabarti, D.E. Laughlin, Phase relations and precipitation in Al–Mg–Si alloys with Cu additions, Prog. Mater. Sci. 49 (3–4) (Jan. 2004) 389–410, https://doi.org/10.1016/S0079-6425(03)00031-8.
[32] C. Ravi, C. Wolverton, First-principles study of crystal structure and stability of Al-Mg-Si-(Cu) precipitates, Acta Mater. 52 (14) (Aug. 2004) 4213–4227, https://doi.org/10.1016/j.actamat.2004.05.037.
[33] K. Matsuda, et al., Precipitation sequence of various kinds of metastable phases in Al-1.0mass% Mg2Si-0.4mass% Si alloy, J. Mater. Sci. 35 (2000) 179–189, https://doi.org/10.1023/A:1004769305736.
[34] L. Arnberg, et al., The crystal structure of Al(x)Cu2Mg(12-x)Si7, (h-AlCuMgSi), Acta Chem. Scand. 34a (1980) 1–5, https://doi.org/10.3891/acta.chem.scand.34a-0001.
[35] S.J. Andersen, C.D. Marioara, J. Friis, S. Wenner, R. Holmestad, Precipitates in aluminium alloys, Adv. Phys. X. 3 (1) (Jan. 2018) 1479984, https://doi.org/10.1080/23746149.2018.1479984.
[36] M. Fiawoo, et al., Formation of multiple orientation relationships of Q precipitates in Al–Mg–Si–Cu alloys, Scr. Mater. 88 (Oct. 2014) 53–56, https://doi.org/10.1016/j.scriptamat.2014.05.013.
[37] C. Wolverton, Crystal structure and stability of complex precipitate phases in Al–Cu–Mg–(Si) and Al–Zn–Mg alloys, Acta Mater. 49 (16) (Sep. 2001) 3129–3142, https://doi.org/10.1016/S1359-6454(01)00229-4.
[38] C.B.L.D.E. Chakrabarti D.J, Precipitation in Al-Mg-Si-Cu alloys and the role of the Q phase and its precursors, in: Proceedings of the 1998 TMS Annual Meeting, San Antonio, Feb. 1998, pp. 27–44.
[39] K. Matsuda, S. Ikeno, Y. Uetani, T. Sato, Metastable phases in an Al-Mg-Si alloy containing copper, Metall. Mater. Trans. A 32 (6) (Jun. 2001) 1293–1299, https://doi.org/10.1007/s11661-001-0219-2.
[40] C. Cayron, L. Sagalowicz, O. Beffort, P.A. Buffat, Structural phase transition in Al-Cu-Mg-Si alloys by transmission electron microscopy study on an Al-4 wt% Cu-1 wt % Mg-Ag alloy reinforced by SiC particles, Philos. Mag. A 79 (11) (Nov. 1999) 2833–2851, https://doi.org/10.1080/01418619908212027.
[41] S.D. Dumolt, D.E. Laughlin, J.C. Williams, Formation of a modified β′ phase in aluminum alloy 6061, Scr. Metall. 18 (12) (Dec. 1984) 1347–1350, https://doi.org/10.1016/0036-9748(84)90362-4.
[42] L. Sagalowicz, G. Lapasset, G. Hug, Transmission electron microscopy study of a precipitate which forms in the Al-Mg-Si system, Philos. Mag. Lett. 74 (2) (Aug. 1996) 57–66, https://doi.org/10.1080/095008396180407.
[43] R. Vissers, M.A. van Huis, J. Jansen, H.W. Zandbergen, C.D. Marioara, S. J. Andersen, The crystal structure of the β′ phase in Al–Mg–Si alloys, Acta Mater. 55 (11) (Jun. 2007) 3815–3823, https://doi.org/10.1016/j.actamat.2007.02.032.
[44] M.H. Jacobs, The structure of the metastable precipitates formed during ageing of an Al-Mg-Si alloy, Philos. Mag. 26 (1) (Jul. 1972) 1–13, https://doi.org/10.1080/14786437208221015.
[45] C. Cayron, P.A. Buffat, Transmission electron microscopy study of the β′ phase (Al–Mg–Si alloys) and QC phase (Al–Cu–Mg–Si alloys): ordering mechanism and crystallographic structure, Acta Mater. 48 (10) (Jun. 2000) 2639–2653, https://doi.org/10.1016/S1359-6454(00)00057-4.
[46] J.G. Barlock, L.F. Mondolfo, Structure of some aluminium-iron-magnesium-manganese- silicon alloys, Int. J. Mater. Res. 66 (10) (Oct. 1975) 605–611, https://doi.org/10.1515/ijmr-1975-661008.
[47] J.S. Kasper, S.M. Richards, The crystal structures of new forms of silicon and germanium, Acta Crystallogr. 17 (6) (Jun. 1964) 752–755, https://doi.org/10.1107/S0365110X64001840.
[48] M. Cooper, The crystal structure of the ternary alloy α(AlFeSi), Acta Crystallogr. 23 (6) (Dec. 1967) 1106–1107, https://doi.org/10.1107/S0365110X67004372.
[49] L. Lodgaard, N. Ryum, Precipitation of dispersoids containing Mn and/or Cr in Al–Mg–Si alloys, Mater. Sci. Eng. 283 (1–2) (May 2000) 144–152, https://doi.org/10.1016/S0921-5093(00)00734-6.
[50] C. Rømming, V. Hansen, J. Gjønnes, Crystal structure of β-Al4.5FeSi, Acta Crystallogr. B 50 (3) (Jun. 1994) 307–312, https://doi.org/10.1107/S0108768193013096.
[51] O. Engler, S. Zaefferer, V. Randle, Introduction to Texture Analysis, CRC Press, Boca Raton, 2023, https://doi.org/10.1201/9781003258339.
[52] P. Lang, E. Povoden-Karadeniz, A. Falahati, E. Kozeschnik, Simulation of the effect of composition on the precipitation in 6xxx Al alloys during continuous-heating DSC, J. Alloys. Compd. 612 (Nov. 2014) 443–449, https://doi.org/10.1016/j.jallcom.2014.05.191.
[53] A. Deschamps, C.R. Hutchinson, Precipitation kinetics in metallic alloys: experiments and modeling, Acta Mater. 220 (Nov. 2021) 117338, https://doi.org/10.1016/j.actamat.2021.117338.
[54] C. Hutchinson, Y. Brechet, A new approach to solid-state nucleation in kinetically-constrained systems, Acta Mater. 283 (Jan. 2025) 120521, https://doi.org/10.1016/j.actamat.2024.120521.
[55] X. Ou, J. Sietsma, M.J. Santofimia, Fundamental study of nonclassical nucleation mechanisms in iron, Acta Mater. 226 (Mar. 2022) 117655, https://doi.org/10.1016/j.actamat.2022.117655.
[56] E. Kozeschnik, Modeling Solid-State Precipitation, Momentum Press, 2012, https://doi.org/10.5643/9781606500644.
[57] J. Van de Langkruis, N.C.W. Kuijpers, W.H. Kool, F.J. Vermolen, S. van der Zwaag, Modeling Mg2Si dissolution in an AA6063 alloy during preheating to the extrusion temperature, in: Proceedings of the 7th International Aluminum ExtrusionTechnology Seminar, Chicago, 2000, pp. 119–124.
[58] J.A. Österreicher, M. Kumar, A. Schiffl, S. Schwarz, G.R. Bourret, Secondary precipitation during homogenization of Al-Mg-Si alloys: influence on high temperature flow stress, Mater. Sci. Eng. 687 (Feb. 2017) 175–180, https://doi.org/10.1016/j.msea.2017.01.074.
[59] B. Sonderegger, E. Kozeschnik, Interfacial energy of diffuse phase boundaries in the generalized broken-bond approach, Metall. Mater. Trans 41 (12) (Dec. 2010) 3262–3269, https://doi.org/10.1007/s11661-010-0370-8.